



Homology modeling of *T. cruzi* and *L. major* NADH-dependent fumarate reductases: Ligand docking, molecular dynamics validation, and insights on their binding modes



Alicia Merlino^{a,*}, Marisol Vieites^b, Dinorah Gambino^b, E. Laura Coitiño^{a,*}

^a Laboratorio de Química Teórica y Computacional, Instituto de Química Biológica, Facultad de Ciencias, Universidad de la República, Igua 4225, 11400 Montevideo, Uruguay

^b Cátedra de Química Inorgánica, Facultad de Química, Universidad de la República, Gral. Flores 2124, C. C. 1157, 11800 Montevideo, Uruguay

ARTICLE INFO

Article history:

Accepted 3 December 2013

Available online 12 December 2013

Keywords:

NADH-dependent fumarate reductase 3D structure

NADH/fumarate binding mode

Trypanosoma cruzi/*Leishmania major*

fumarate reductases inhibitors

Anti-trypanosomatids rational design

Computational modeling

ABSTRACT

Leishmania major and *Trypanosoma cruzi* are the main causes of leishmaniasis and Chagas disease, two endemic parasitosis identified as neglected diseases by the World Health Organization. Fumarate reductase (FR) is a central enzyme in the conversion of fumarate to succinate, an energy releasing path essential for the survival of these protozoans which is also absent in their mammalian hosts. FR can thus be considered as a good candidate for targeting specific inhibition by new drugs designed against *L. major* and *T. cruzi*. The lack of tertiary structures available for *LmFR* and *TcFR* has limited until now the possibility of performing structure-based drug design. Here we used homology modeling combined with enzyme-cofactor docking to propose tertiary structures for NADH-dependent *LmFR* and *TcFR* using an homologous X-ray crystallographic structure of flavine-adenine dinucleotide (FAD) dependent FR from *Shewanella frigidimarina* (PDB ID: 1QO8) as template. These models were refined and stabilized with/without substrate in the active site using classical molecular dynamics simulations under quasi-physiological conditions. Structural features relevant for understanding the mechanism of action of the enzyme were also analyzed, with special attention to the hydrogen bond network involving the cofactor and water molecules present at the binding sites. A small set of compounds previously synthesized and assayed for their inhibitory capacity against *TcFR* ([M(mpo)₂] metal complexes with M = Pt^{II}, Pd^{II} and V^{IV}O and mpo = 2-mercaptopyridine *N*-oxide) and *LmFR* (licochalcone A) were screened by protein–ligand docking using the NADH-*LmFR* and NADH-*TcFR* models here proposed and validated, gaining insight into their binding modes in each enzyme.

© 2013 Elsevier Inc. All rights reserved.

1. Introduction

American Trypanosomiasis (Chagas disease, CD) and leishmaniasis are infectious illnesses designated by the World Health Organization as neglected tropical diseases. Their causative agents, *Trypanosoma cruzi* and *Leishmania* spp., are genetically related protozoa parasites belonging to the family Trypanosomatidae and order Kinetoplastida which are mainly transmitted to mammalian hosts through the bite of certain insects [1]. Chagas disease constitutes a major health problem, being prevalent in Latin America [2].

Abbreviations: FR, fumarate reductase; *LmFR*, *Leishmania major* fumarate reductase; *TcFR*, *Trypanosoma cruzi* fumarate reductase; mpo, 2-mercaptopyridine *N*-oxide; CD, Chagas disease; SD, steepest descent; CG, conjugate gradient.

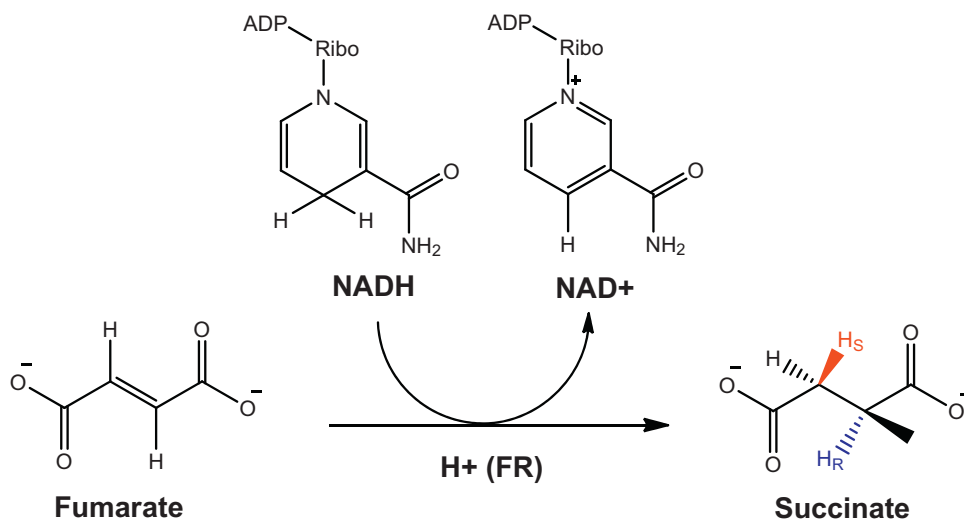
* Corresponding authors at: Theoretical & Computational Chemistry Lab., Institute of Biological Chemistry, Faculty of Sciences, University of the Republic, Igua 4225, Montevideo 11400, Uruguay. Tel.: +598 25252186; fax: +598 25250749.

E-mail addresses: amerlino@fcien.edu.uy, amerlino@adinet.com.uy (A. Merlino), laurac@fcien.edu.uy (E. Laura Coitiño).

Transfusion of infected blood and congenital infection are alternative ways of transmission for the parasites [3]. Globalization and immigration of infected people from Latin America has led to the appearance of several infection cases in developed countries, mainly due to the lack of controls and screening in blood and organ banks [2]. Recent reports also indicate that the disease turned to be a potential public health problem in the US and Western Europe [4,5].

Leishmaniasis identifies a group of diseases produced by different protozoa of the genus *Leishmania*. It affects about 12 million people worldwide with 1.5–2 million new cases per year, including approximately 500 000 cases of the visceral form of the disease, which is nearly 100% fatal when untreated. Leishmaniasis is prevalent in 88 countries in Africa, South Asia, and Latin America. In recent years the disease has also increased its prevalence in the south of Europe due to co-infection of patients affected by HIV-AIDS [6].

Chemotherapy of trypanosomatid infections mostly relies on drugs that date back over 50 years, suffering from poor efficacy,



Scheme 1. Fumarate conversion to succinate as catalyzed by NADH-dependent fumarate reductase (FR). Whereas the cofactor would act as source of hydride attacking the central double bond in the substrate, the protein would provide a proton from the opposite side leading to formation of the product of reduction (succinate) [25].

high toxicity, and increasing resistance. The treatment of CD has been based for years on old and quite unspecific nitroheterocyclic drugs (nifurtimox and benznidazole) whose activity is significant just in the acute phase of the disease and give rise to severe side effects when associated with long-term treatments [7,8]. Their use during the chronic phase of the disease is still controversial, because of their toxicity, potential carcinogenic properties, and variable efficacy [9]. Recent reviews on the chemotherapy of CD stressed deficiencies of the current therapeutic agents as well as the urgent need for new improved therapeutic candidates [10,11]. The available treatments for leishmaniasis are also far from being ideal. The first-line treatment traditionally relies on the pentavalent antimonial drugs sodium stibogluconate and meglumine antimoniate. These antimonials may also cause severe side effects and development of resistance has been observed in several cases and geographical regions [12,13].

Side effects associated to current treatments against both diseases have promoted the development of novel chemotherapeutic approaches, based on biochemical pathways and enzymes which are specific for the parasites [14–16]. Among them, soluble NADH-dependent fumarate reductase (NADH-FR, EC 1.3.1.6) was shown to be present in several members of the genus *Trypanosoma* [17–20] and has been shown to be a promising target [21–24]. Fumarate respiration is a key process in the anaerobic energy metabolism of the parasites, required to grow and survive in their host. The enzyme is responsible for catalyzing the energy generating conversion of fumarate to succinate using $2\text{H}^+/2\text{e}^-$ at the active site (see Scheme 1) and is absent in normal cells of the mammalian host [25] (although recent reports point out the presence of mitochondrial NADH-FR in tumor microenvironments [26]).

Although this would make FR an ideal pharmacological target for designing very specific antiprotozoals, one of the main drawbacks in undertaking a rational design of NADH-FR inhibitors has been the lack of an experimentally determined 3D structure of *TcFR* and *LmFR*. In fact, since the discovery circa twenty years ago of *TcFR* as a potential target [17], very few novel inhibitors have been proposed. A first line of compounds against *T. cruzi* fumarate reductase (*TcFR*) reported in the late 90s comprised a series of imidazole derivatives [21] and the drug 2-mercaptopyridine *N*-oxide (Hmpo) [22]. More recently, bis(2-mercaptopyridine *N*-oxide) platinum(II) and palladium(II) complexes (see Fig. 1D and E) have been reported to be more potent inhibitors of *TcFR* [27]. However, their putative binding sites and mechanism of inhibition remain unknown. On the other

side, the only species reported up to now as effective inhibitors of *L. major* fumarate reductase (*LmFR*) are licochalcone A (see Fig. 1C) and related chalcones [23] and aurones [24] but, as for the former series of compounds, the detailed mechanism of inhibition has not been determined yet.

In this study we performed homology modeling, protein–ligand docking, and molecular dynamics simulations combined to obtain trustworthy 3D models of *TcFR* and *LmFR* bound to NADH. The models thus obtained were used to predict and analyze the features of the binding mode of the cofactor and substrate (fumarate) into both enzymes. We also explored the binding mode of $[\text{Pt}(\text{mpo})_2]$ and $[\text{Pd}(\text{mpo})_2]$ into *TcFR* and licochalcone A into *LmFR*. Moreover, the inhibitory capacity of the metal complexes on *LmFR* was also assessed. Finally, a related oxidovanadium complex bis(2-mercaptopyridine *N*-oxide) oxidovanadium(IV), $[\text{VO}(\text{mpo})_2]$ (Fig. 1F) with potential anti-parasitic activity [28] was screened *in silico* against both enzymes.

2. Computational methods

2.1. Homology modeling of ligand-free *LmFR*/*TcFR*

The amino acid sequence of *LmFR* and *TcFR* (accession numbers E9AEQ8 and Q4CYX1, respectively) was retrieved from the Swiss-Prot database [29]. BLAST-P [30] was used to identify homologous structures by searching the structural database of protein sequences in the Protein Data Bank. Based on the highest percentage of sequence identity and similarity of alignment (34% identity and 50% similarity for *LmFR* and *TcFR*) the crystal structure of the marine bacterium *Shewanella frigidimarina* soluble FR (PDB ID: 1QO8, chain A) was selected as structural template for the homology modeling of both target enzymes, preferred over another soluble flavocytochrome FR structure from *Shewanella putrefaciens* (PDB ID: 1D4C) that also emerged as a potential template, with 34–35% sequence identity against *LmFR* and *TcFR* (all the four amino acid sequences were compared for conserved regions by multiple alignment with CLUSTALW [31]). BLAST results showed a total score of 241 and an E-value of 5×10^{-68} between *LmFR* and 1QO8 and of 244 and 6×10^{-69} between *TcFR* and the *Shewanella frigidimarina* template. The SWISS-MODEL server [32] was used to generate the corresponding models. The root mean square deviations (RMSDs) of the models relative to the template (PDB ID: 1QO8) were calculated using SuperPose [33]. The overall stereochemical quality of

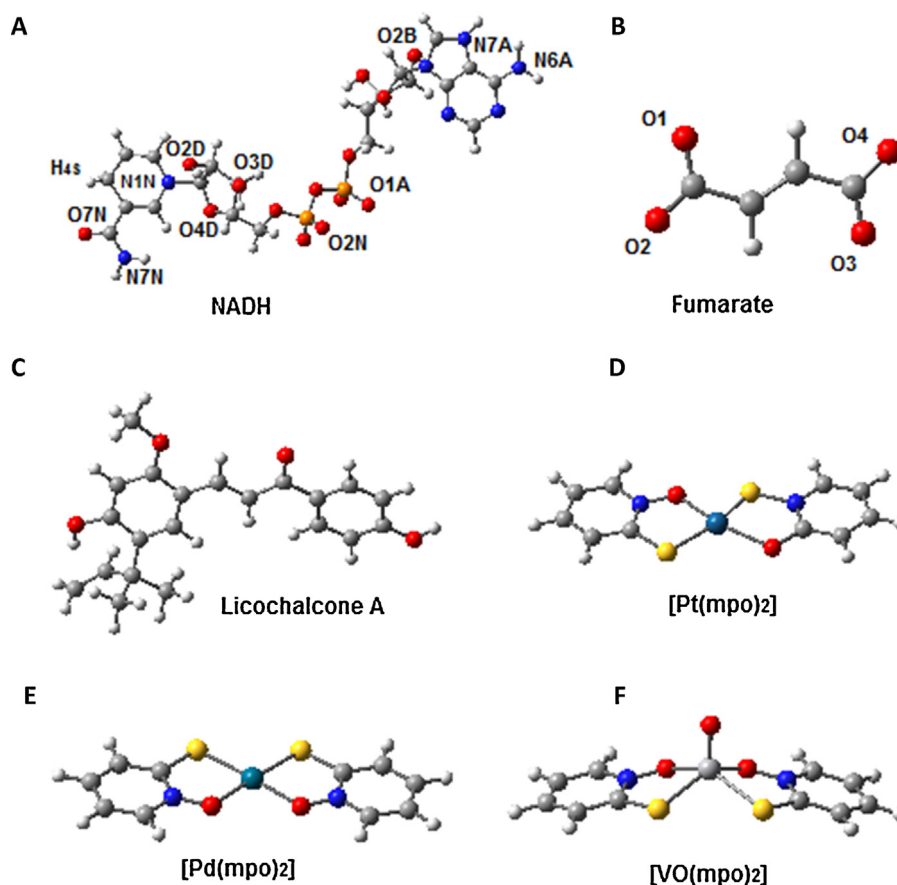


Fig. 1. Chemical structure of the species considered as protein ligands in this study (from left to right, up to bottom): (A) cofactor NADH with relevant atoms labeling; (B) substrate fumarate; (C) known *LmFR* inhibitor, Licochalcone A; (D) known *TcFR* inhibitor, *trans*-[Pt(mpo)₂]; (E) known *TcFR* inhibitor, *cis*-[Pd(mpo)₂]; (F) potential *TcFR/LmFR* inhibitor, *cis*-[VO(mpo)₂].

the developed models was assessed by using PROCHECK [34a] and Molprobit [34b] and the environment profile was checked using Verify-3D [35].

2.2. Refinement of the models with classical methods

In order to improve the stereochemical quality of the homology models, they were subjected to energy minimization with molecular mechanics using the *ff03.r1* force field [36] within the AMBER 12 package [37]. Optimization of the structures by energy minimization was performed in implicit water solvent modeled by a modified Generalized Born method developed by Onufriev et al. [38] with a cutoff of 30 Å for non-bonded interactions. Different amounts of minimization steps were tested for an adequate convergence. 5000 minimization steps (500 steepest descent steps, SD, and 4500 conjugate-gradient steps, CG) were sufficient to obtain a good quality model of *TcFR*. For *LmFR* the best results were obtained after 1500 minimization steps (500 SD and 1000 CG). The quality of the models was assessed as described in Section 2.1.

2.3. Protein–ligand docking models

The molecular structure of the cofactor, substrate, and each of the ligands used to feed the protein–ligand docking studies are illustrated in Fig. 1. Fumarate, licochalcone A, and the three metal complexes were fully optimized *in vacuo* at the density functional theory (DFT) level using the BP86 GGA functional [39,40] with the 6–31+G(d,p) [41,42] basis set for H/C/N/S/O atoms and the LANL2DZ pseudopotential and associated basis set [43,44] for Pt(II)/Pd(II)/V transition metals. A fully unrestricted formulation

was employed for the open-shell oxidovanadium(IV) complex. The nature of the optimized structures as stable species was carefully inspected checking the *eigenvalues* of the analytic Hessian matrix calculated at the same level of theory to be positive in all the cases. All these calculations were performed using the Gaussian09 suite [45]. The structure of NADH was extracted from the crystal structure of rabbit muscle lactate dehydrogenase (PDB ID: 3H3F). NADH was docked into the refined structure of each of the 3D ligand-free FR proteins as predicted by homology modeling. Fumarate, licochalcone A, and the three metal complexes were docked into averaged structures of *NADH-TcFR/NADH-LmFR* complexes obtained over MD simulations (see Section 2.4). AutoDock 4.2 empirical free energy function and a Lamarckian Genetic Algorithm were used for all the docking calculations and the AutoDockTools (ADT) package was used to generate input files and to analyze results [46]. Gasteiger-Marsilli charges were used and parameters for Pt^{II}, Pd^{II}, and V^{IV} were included in AutoDock's parameters file (R_{ii} and ϵ_{ii} values for Pt^{II}/V^{IV} metal ions were based on AutoDock parameters for transition metals [47] and a set of parameters developed by Divsalar et al. were used for Pd^{II}, where $R_{ii} = 2.50$ and $\epsilon_{ii} = 0.458$ [48]). Since the precise location of NADH and ligands in the protein was unknown, a grid map of $126 \times 126 \times 126$ points spaced by 0.65 Å was applied to explore the entire protein surface, with the maps initially centered on the macromolecule. Once the binding site was determined, the free energies of binding were refined using a smaller grid box, sized $60 \times 60 \times 66$ points with a spacing of 0.375 Å, now centered at the ligand binding site. In docking fumarate to cofactor-enzyme complexes, a grid box of $20 \times 20 \times 20$ point with a spacing of 0.375 Å was employed, centered at the C4 position of the nicotinamide ring of NADH. Each docking experiment consisted of 50 independent

runs, with an initial population of 300 individuals and a maximum of 2.5×10^6 energy evaluations and 27,000 generations. Mutation and crossover were applied to the population at rates of 0.02 and 0.80, respectively. The pseudo-Solis and Wets method was used for the local search, with translational and orientational/torsional step-sizes of 0.2 Å and 5.0° , respectively. For the remaining parameters, AutoDock 4.2 default values were used. Results differing by less than 2.0 Å in root-square-deviation were grouped into the same cluster. In all cases, we filtered out docking results by selecting the best scored docking pose from the most populated cluster, also checking the predicted binding modes for NADH were similar to that known for FAD in related and well-characterized FRs.

2.4. Structural refinement with molecular dynamics simulations and H-bond analysis

MD refinement and validation of the structure of binary/ternary complexes established by the proteins with both NADH and NADH + fumarate was performed with *sander* in AMBER 12 suite [37], using the *ff03.r1* force field for proteins [36] and *gaff* for the ligands [49]. Parameters for NADH were taken from AMBER database [50]. Partial charges for fumarate were obtained according to the restrained electrostatic fit (RESP) scheme [51] (electrostatic potentials calculated by HF/6-31G* single-point calculations on the DFT geometries obtained as described in Section 2.3). H atoms and K⁺ ions (to neutralize charge) were added to the complexes with the *leap* utility. Each complex was placed in a truncated octahedral box of TIP3P explicit water [52], extended 10 Å outside the protein on all sides. The structure of each solvated complex was optimized as follows: (a) water and ions were relaxed to minimize energy during 2000 steps (500 SD and 1500 CG) with the protein frozen with a 500 kcal mol⁻¹ Å⁻² restraint applied; (b) all the system was minimized without restraints during 15,000 steps (5000 SD and 10,000 CG). A cut-off radius of 10 Å was applied for non-bonded interactions and long-range electrostatics was treated using the particle-mesh Ewald (PME) method [53] with a grid spacing of 1 Å. After minimization, the system was gradually heated in a NVT ensemble from 0 to 300 K over 20 ps, keeping the protein fixed with a constraint of 10 kcal mol⁻¹ Å⁻². 20 ps of equilibration were carried out without restraints, followed by 1 ns of NPT simulation with $T = 300$ K and $P = 1$ atm (the effect of using longer simulations was also assessed, not finding significant differences for the scope of this study). Temperature and pressure were, respectively, controlled by using the Langevin coupling scheme [54] and the isotropic position scaling protocol as applied in AMBER 12. All covalent bonds including H atoms were constrained using SHAKE [55]. The time step of simulation was set to 2.0 fs. After equilibration, coordinates of the complexes were saved every 0.2 ps. Representative structures averaged over the 300–1000 ps time frames were generated for both NADH-*TcFR* and NADH-*LmFR* and their complexes with the substrate by using the *ptraj* utility in Amber Tools 12 [37]. The same utility was used to analyze geometrical parameters and hydrogen-bond interactions, applying thresholds of 3.2 Å for acceptor(A)–donor(D) distances and 120° for D–H...A angles as geometrical criteria for defining presence/absence of HB interactions.

2.5. *LmFR* and *TcFR* sequences pre-analysis using bioinformatics web tools

The structural modeling was also complemented with a pre-analysis of the *LmFR*/*TcFR* sequences conducted using web server tools SignalP 4.1 [56], PROlocalizer [57], Minnou [58], and MitoProt II [59] in search of signal peptides (SP), *trans*-membrane regions (TM), and mitochondrial signals (mTP). All the predictors

are consistent in pointing out the absence of any TM in both proteins. Concerning their subcellular localization, whereas *TcFR* is predicted to be found in the lumen of the endoplasmic reticulum (with a probability of export to mitochondria higher than 0.7, a feature shared with most of the available *T. brucei* FR sequences but FRDg Q5BU13 [20]) *LmFR* is predicted to partially localize in the mitochondrial matrix with chance of being also loosely associated to the plasma membrane after myristoylation at Gly2 (as confirmed by the NMT-Predictor [60] reporting a cleavage site at position 13 in the sequence). No evidence of glycosomal PTS1 targeting signals (positive for TbFR FRDg Q5BU13 [20]) is found for *LmFR* and *TcFR* sequences.

Secondary structure, domain, and disorder analysis were also conducted by applying PsiPred [61] and Disopred [62] through the Phyre² engine [63] on the complete sequences of the proteins. Hybrid (integrating homology, threading, and *ab initio*) multiple-template modeling was also conducted using the complete sequences with the intensive protocol in Phyre² [63]. Overall 3D structures for both proteins (92% and 90% of the corresponding sequences, modeled at >90% accuracy respectively for *LmFR* and *TcFR*) were thus obtained (see Fig. S1 in the Supporting Information). This enabled to assess the main features of the extended regions of both proteins (excluded in the single-template homology models constructed as described in Section 2.1) and to validate the use of a reduced 3D model in further characterizing the nature and location of the active site and its interactions with ligands. N/C-terminal regions appear as independent domains in both proteins, disposed far from the conserved residues presumed to be part of the NADH-FR active site and displaying a mixed secondary structure with highly disordered segments at the core and in the hinge regions connecting to the central domains.

3. Results and discussion

3.1. Homology models: evaluation and refinement

The crystal structure corresponding to chain A of *Shewanella frigidimarina* (PDB ID: 1QO8) was selected as potential template for both enzymes as the result of BLAST-P [30] search conducted for *LmFR* and *TcFR*. Although the *Shewanella frigidimarina* template only covers the central domain of the two parasitic FRs (residues 452–950 in *TcFR* and 432–930 in *LmFR*) the segment includes both the known catalytic and FAD binding sites of *S. frigidimarina* [64].

Multiple alignment of two soluble bacterial FRs against the two targets shows that the amino acids forming the catalytic site, binding the cofactor, and properly positioning residues in direct contact with them (highlighted in red and green, respectively, in Fig. 2) are well conserved. Recalling the N/C-terminal domains missing in the single-template models are placed far enough from these sites (see Section 2.5) it is also unlikely that significant interactions among them capable of modifying the overall picture are missing here. Therefore these partial models based on PDB ID: 1QO8 as template appear to be good approaches to get insight into the catalytic mechanism of these NADH-dependent enzymes and to understand and predict the efficiency of potential FR inhibitors.

A 3D overlay of the two models and the template is shown in Fig. 3. Domains identified as 2 and 3 exhibit a strong structural conservation (C_α RMSD values of 0.54 and 0.81 Å for *TcFR* and *LmFR* with respect to the template) corresponds to the FAD/NAD cofactor and substrate binding domains. Domain 1, corresponding to the heme binding domain in *Shewanella frigidimarina*, displays no homology with *TcFR* nor *LmFR*.

The high similarity in sequence among *TcFR*, *LmFR*, and soluble FRs (not found against the flavoprotein subunit of membrane-bound complex II FR analogs from *E. coli* [65] and *W. succinogenes*

<i>S. frigidimarina</i>	ATAAGPSETTQVLVVGAGSAGFNASLAACKAGANVIL	DIAPFSGGNSMI	162
<i>S. putrefaciens</i>	ATAAGVKETTDVVIIGSGGAGLAAAVSARDAGAKVILL	ETEPIDPGNTKL	167
<i>L. major</i>	----AGSLPARVVVIGGGLAGCAAIEAASCATVILL	ETEARLGGNSAK	477
<i>T. cruzi</i>	----AGSLPARVIVVGGGLAGLSAAIEATACGAQVILL	ETEPKVGNSAK	497
<i>S. frigidimarina</i>	SAGGMNAVGTQQTAAHGVEDKVEWFIEDAMKGGRO-QNDIKLVITILAEQS		211
<i>S. putrefaciens</i>	AAGGMNAAETKPAQKLGIEDKKQIMIDDTMKGGRN-INDPELVKVLANS		216
<i>L. major</i>	ATSGINGWGTRTQAVNHVLDNCKFFERDTFLSGKGHCDPGLVRTLSVKS		527
<i>T. cruzi</i>	ATSGINGWGTRAQALDDIQDNCNIFERDTHKSGLGSTVPSLVRTLVS		547
<i>S. frigidimarina</i>	ADGVQWLES LGANLDDLKRSGGARVDRTHRPHGGKSSGPEIIDT-----		255
<i>S. putrefaciens</i>	SDSIDWLTSMGADMTDVGRMGASVNRSHRPTGGAGVGHAHVQ-----		260
<i>L. major</i>	AEAISWLESFGIPLTVLYQLGGASRRRCHRAPDQKDGTPVPVGF-----		571
<i>T. cruzi</i>	GDAISWLSSLGVPLTVLSQLGGHSRKRTHRPAKADGTPVPVIGF-----		591
<i>S. frigidimarina</i>	----LRKAAKEQGIDTRLNSR	VKLVDNDH-----SVV	285
<i>S. putrefaciens</i>	----LWDNAVKGRTDIRLNSR	VRILEDASG-----KVT	290
<i>L. major</i>	----TIMRHLEDHIRTKLQGR	VILNEMAVVSLMHDVSAMPDGNREIRVH	617
<i>T. cruzi</i>	----TIMRTLEQHVRTKLADP	VIMENTLVTSLLHEIKGTPDGGREVRVT	637
<i>S. frigidimarina</i>	GAVVHG---KHTGYMIGAKSVVLATGGYGMN---KEMIAYYRPTMKDMT		329
<i>S. putrefaciens</i>	GVLVKG---EYTGYYVIKADAVVIAAGGFAKN---NERVSKYDPKLKGF		334
<i>L. major</i>	GVRYSMTDASGTVMIDLPAVVLATGGFSNDRTPNSSLREYAPNVYGT		667
<i>T. cruzi</i>	GVTYKNSDEKETSSMKLTADAVILATGGFSNDHMSQSLIGEFAPELSGFP		687
<i>S. frigidimarina</i>	SSNITATGDGVLMKEIG-ASMTDIDWVQA	HPT-----VGKDSRILI	371
<i>S. putrefaciens</i>	ATTHPGATGDGLDVALQAG-AATRDLEYIQ	HPT-----YSPAGGVMI	376
<i>L. major</i>	TTTGTFATGDGVKMARKLG-ATLVDMKVQI	HPTGLIDPKDPSNRKTYLG	716
<i>T. cruzi</i>	TTTGFWATGDGVKLARRLG-ATLVDMKVQI	HPTGLIDPKDPANPTKYLG	736
<i>S. frigidimarina</i>	SETVRGGVAVMVNKGDNRFISELTTR	KASDAILKQPGQF-----AW	413
<i>S. putrefaciens</i>	TEAVRNGAIVVNREGNRFMNEITTR	KASAAILQKKGES-----AY	418
<i>L. major</i>	TEALRGSGGILLNKNGERFVNELDR	SVVSQAI IAQDNEYPNSSGSKFAY	766
<i>T. cruzi</i>	TEALRGSGGVLLNKKGERFVNELDR	SVVSNAIIEQGDEYPYSGSKFAF	786
<i>S. frigidimarina</i>	IIFDNQLYKKAKMVRG---YDHLEMLYKGDTPVEQLAKSTGMKVADLAKTV		460
<i>S. putrefaciens</i>	LVFDDSIKSLKAIEG---YVHLNIVKEGKTIEELAKQIDVPAELAKTV		465
<i>L. major</i>	CVLNEEAATLFGKNSLTYYWKSQGLFTRVDDMKALAEIGCSVESLHRTL		816
<i>T. cruzi</i>	CVLNDAAVELFGVNLLNFYANTLGVFKRVDDLQGLAMLIGCDVLTQLNTL		836
<i>S. frigidimarina</i>	SDYNGY--VASGKDTAFGRADMPLNMT--QSPYYAVKVAPG	HPTMGGVA	506
<i>S. putrefaciens</i>	TAYNGF--VKSQKDAQFERPDLPREL--VAPFYALEIAPV	HPTMGGLV	511
<i>L. major</i>	ETYERQ--STGKKACPLTGKLVFSPVVGTKGPYYVAVVTPS	HPTMGGCF	864
<i>T. cruzi</i>	EAYESN--SIATSACPFTEKVVYPCVLGPQGPFFVAFVTPS	HPTMGGCL	884
<i>S. frigidimarina</i>	INTTASVL-----DLQS-KPIDGLFAAC	ETGGVHGE	548
<i>S. putrefaciens</i>	IDTKAEVK-----SEKTGKPIITGLYAAE	ETGGVHGE	554
<i>L. major</i>	ISPAEELLMEDHSVNI FDDMRPILGLFGAC	ETGGVHGE	914
<i>T. cruzi</i>	ISPSAEIQREHHSNLLENQRPILGLFGAC	ETGGVHGE	934
<i>S. frigidimarina</i>	VVFGRIAGDNAAKHALDK-----		566
<i>S. putrefaciens</i>	VTYGRIAGASAAKFAKDN-----		572
<i>L. major</i>	VVFGKIAGDNAAKHAL-----		930
<i>T. cruzi</i>	VVFGRIAGDNAAKHAL-----		950

Fig. 2. CLUSTALW multiple alignment among NADH-dependent target sequences and soluble FADH₂-dependent bacterial flavoprotein subunits of FR. Residues involved in cofactor binding and catalysis are, respectively, evidenced in green and red, in vertical boxes. (For interpretation of the references to color in this figure legend, the reader is referred to the web version of the article.)

[66], displaying 28% and 25% of identity) suggests the parasitic enzymes are soluble proteins, as already shown for one of the *T. brucei* NADH-FRs (*TbFR*) [19]. Accordingly, the identity percentages between the *TbFR-TcFR* and *TbFR-LmFR* pairs are 63% and 58%, respectively. After assessing their quality (see Figs. S2 and S3 in the Supplementary Material), the homology 3D-models were refined by following the protocol described in Section 2.2. Inspection of the Ramachandran plots for both protozoan enzymes (Fig. S2) confirmed that 99% of the residues are placed in favored or in additional allowed regions. A couple of residues in *TcFR* (representing 0.5% of the model) correspond to disallowed regions, but since they are not involved in catalysis or cofactor binding, it is possible to consider the model reliable enough to proceed with the enzyme-cofactor docking. A compatibility score greater than 0.2 in the Verify-3D graph (see Fig. S3 in the Supplementary Material) implies acceptable side-chain environments. This analysis suggests that the models have overall self-consistency in terms of sequence-structure compatibility.

3.2. Enzyme-cofactor docking and MD refinement and validation

The binding mode of NADH as predicted for the parasitic enzymes is illustrated in Fig. 4. According to the structures obtained by docking both enzymes bind the cofactor in a cleft placed between domains 2 and 3, adjacent to the binding site of FAD in the homologous bacterial FRs. NADH appears to be retained in these sites, stabilized by a hydrogen bond (HB) network involving several residues from both domains. The list includes HB donor-acceptor pairs of atoms as follows (see NADH atom labeling in Fig. 1A):

- O_{2B} from the adenosyl ribose moiety with the main chain oxygen from P731 in *TcFR* (T669 in *LmFR*); adenine's N₇ with N_ε from K497 in *TcFR* (or -NH from the backbone at L715 in *LmFR*);
- O_{1A} and O_{2N} at the pyrophosphate moiety display the same HB motif in both enzymes, that is, H-bonded to T499(T479), NH₁ from R925(R905), and N_{ε2} of H877(H857);

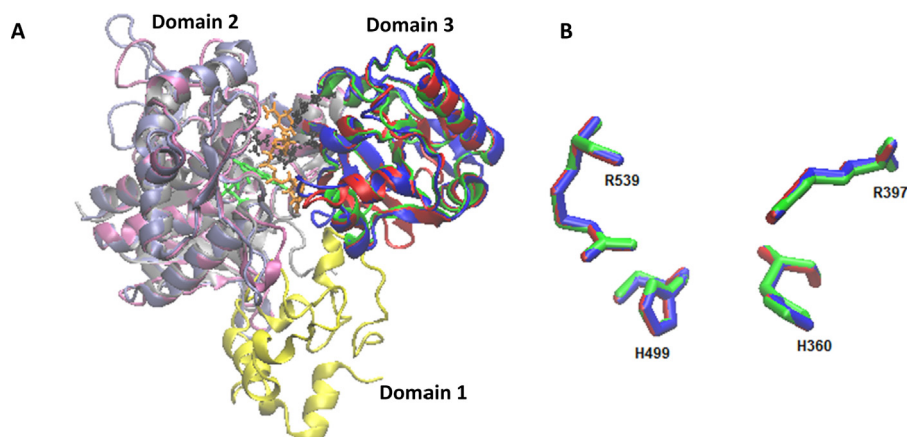


Fig. 3. (A) *TcFR* and *LmFR* models overlaid on the structure of *S. frigidimarina* FR (PDB ID: 1QO8). Domain 1 of the template displays no homology with the parasitic models (bottom, yellow). Domain 2, in the left, corresponds to the FAD/NAD binding domain with a clear structural homology (*TcFR*: skyblue; *LmFR*: mauve; 1QO8: gray; FAD/NAD cofactors in green/orange sticks, respectively). Domain 3, in the right (*TcFR*: blue; *LmFR*: red; 1QO8: green) shows a good superposition among template and models. In bacterial FRs domain 3 is part of an extended solvent channel which encompasses the enzyme active site. (B) Close-up view of Domain 3 with the conserved residues at the active site numbered as in the template. Same color coding as in (A). (For interpretation of the references to color in this figure legend, the reader is referred to the web version of the article.)

- O_{4D} at the nicotinamide ribose's moiety with $-NH_2$ of R925(R905) from both FRs; O_{2D} at the same ribose interacts with both $-NH_2$ and $-NH_1$ groups of R762(R742); polar atoms from the 3-carboxamide group establish HB with N924(N904) and R925(R905) whereas N_{1N} from the nicotinamide's ring is H-bonded to NH_1 from R762(R742).

In both enzymes, a highly conserved R762(R742) residue would be properly positioned to serve as a proton donor to fumarate

during the catalytic cycle (similar roles have already been described for R401 in *S. putrefaciens* FR [67] and for R402 as a part of a proton transfer pathway also involving Glu378 and Arg381 in *S. frigidimarina* [68]). The values of the free energy of binding predicted from these NADH-FR complexes from ligand–protein docking are -7.9 ± 2.5 kcal mol $^{-1}$ for *TcFR* and -7.7 ± 2.5 kcal mol $^{-1}$ for *LmFR*, being consistent with the range of experimental values (-6.5 to -8.3 kcal mol $^{-1}$) covered by NADH binding energies in dehydrogenases [69,70].

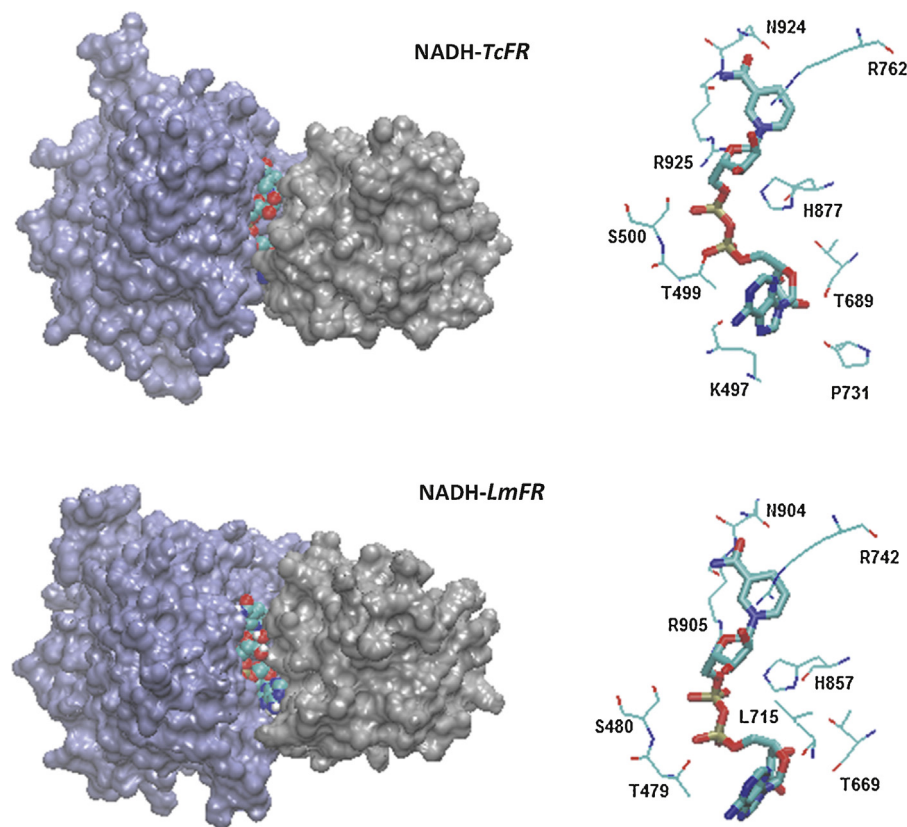


Fig. 4. Predicted binding mode of NADH to the FR models. Upper and bottom representations correspond to *TcFR* and *LmFR*, respectively, showing the solvent accessible surface area (SASA) for Domains 2 and 3 in the left side (Domain 2: iceblue; Domain 3: silver; NADH represented as a vdW spheres) and the corresponding close-up views evidencing contact residues within 3.2 Å around the cofactor in the right (the labels reflect the numbering scheme corresponding to each FR).

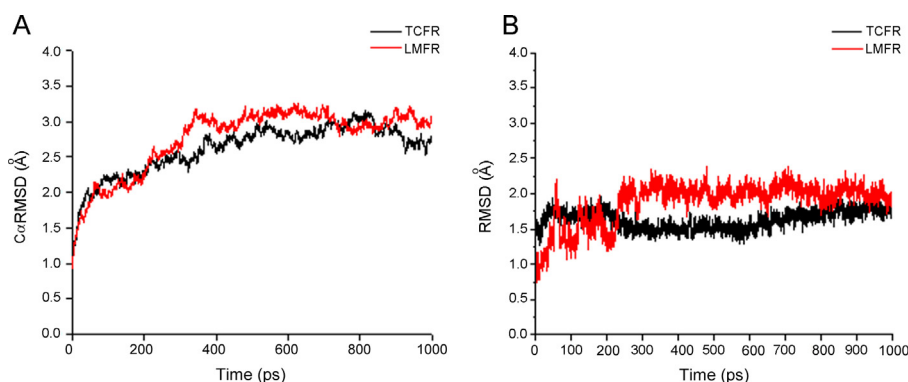


Fig. 5. RMSD along the MD trajectories obtained for NADH-*TcFR* (black) and NADH-*LmFR* (red) complexes. (A) Backbone C_{α} atoms RMSD relative to the initial structure; (B) NADH RMSD profile along the simulation for the two systems relative to the initial structure. (For interpretation of the references to color in this figure legend, the reader is referred to the web version of the article.)

NADH-FR cofactor–enzyme complexes were further refined by using MD simulations under the conditions described in Section 2.4, enabling thus to verify the conformational stability of NADH in the predicted binding sites. As shown in Fig. 5A, the protein backbone (followed through C_{α} RMSD profiles relative to each initial structure) reaches the equilibrium after 300 ps in both NADH-FR complexes, remaining stable (RMSD fluctuations smaller than 0.5 Å) during the rest of the simulations. RMSD averages of 2.8 and 3.0 Å, respectively, obtained for *TcFR* and *LmFR* complexes show that their overall conformation experiences significant alterations with respect to the starting structures obtained by docking, a fact promptly confirmed in further detail from the structural superposition displayed in Fig. 6. The RMSD values obtained for NADH (Fig. 5B) decrease to 1.6 Å in *TcFR* and increase to 2.0 Å in *LmFR* after 300 ps and then level off until the end of the simulation.

The stereochemical quality of each NADH-enzyme complex structures as obtained from averaging over the 300–1000 ps simulation snapshots, was assessed by producing the Ramachandran plots (shown as C and D in Fig. 2S, Supplementary Material) which display minor differences relative to those observed for the corresponding apo-enzyme, with a percentage of 98% of the residues in favored regions in both cases.

A more detailed notion of the structural changes resulting from mutual adaptation at the cofactor binding site is obtained by comparing docking (red) and MD averaged (green) complexes shown in Fig. 6. Local conformational changes implying reorientation of the NADH moiety in both enzymes are readily reached, with very small RMSD fluctuations after 300 ps. The change mainly affects the adenosyl end of the cofactor, which adopts a more extended conformation whereas the protein residues hypothesized to be relevant for the catalytic mechanism (R762 or R742 in *TcFR* and *LmFR*, respectively) become disposed in a similar way as it has been reported for the case of FAD-dependent soluble FRs [25,64,67,68,71].

In order to analyze the dynamic behavior of the interactions established by the cofactor within the binding site, NADH-enzyme hydrogen bonds were monitored and the results summarized in Table 1. Interestingly, most of the HB interactions found in the docked complexes remain along the whole trajectory. Additionally, several water molecules appear to take part in stabilizing the cofactor in the binding site, with HB occupancies higher than 50% during the 700 ps time frame under consideration.

Hydrogen bonds established between NADH and N924, R925(R905) and T499(T479) residues display occupancies of circa 80–90%, supporting the idea that these amino acids might be required for binding the cofactor to the enzyme. Residue N924 and water molecules interact with the 3-carboxamide group in NADH, enabling a proper positioning of atom H_{45} (see Fig. 1A)

for an eventual hydride transfer to happen from the cofactor to the substrate. This is in close resemblance to the mechanistic proposal advanced in explaining catalysis for several soluble FAD-dependent fumarate reductases [25,64,67,68,71]. It is worth to recall here that during the simulation R762(R742) moves toward

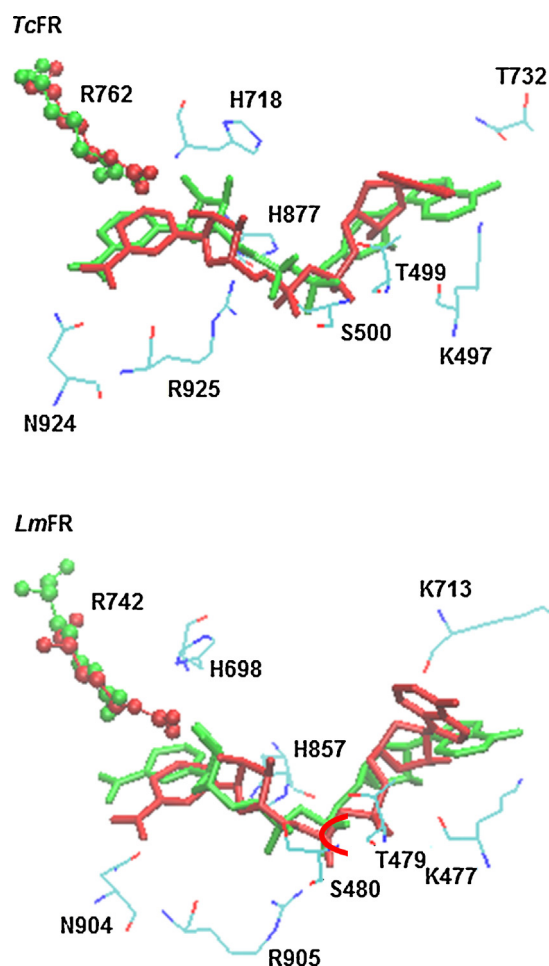


Fig. 6. NADH-FR averaged structures from equilibrated MD simulations (green) superimposed to ligand–protein docking structures (red) for both parasitic enzymes (*TcFR* up, *LmFR* bottom) at their cofactor binding sites. For the sake of clarity only major changes in R762/R742 and the cofactor, respectively, depicted in ball & sticks, are superimposed. Positioning of other residues within 3.2 Å from NADH after running MD simulations is included as line representation, colored by element. (For interpretation of the references to color in this figure legend, the reader is referred to the web version of the article.)

Table 1
Hydrogen bond contacts between NADH and FR from MD simulations.

Complex	H-donor ^{a,b} (residue-atoms)	HB-acceptor ^a (residue-atoms)	Distance (Å)	Angle (°)	Occupancy (%)
NADH- <i>TcFR</i>	N924-Nδ2	NADH-O7N	3.0 ± 0.2	158.98 ± 11.25	90.04
	R925-NH ₂	NADH-O2N	2.9 ± 0.2	150.26 ± 13.83	84.65
	T499-Oγ1	NADH-O1A	2.7 ± 0.1	164.28 ± 10.93	79.80
	R762-NH₂	NADH-O2D	3.0 ± 0.2	138.89 ± 10.55	65.36
	R925-NH ₁	NADH-O2N	2.8 ± 0.2	153.93 ± 12.36	61.94
	R762-NH₁	NADH-O2D	3.0 ± 0.2	141.87 ± 11.61	46.69
	R762-NH₂	NADH-N1N	3.3 ± 0.1	145.06 ± 14.16	38.42
	R762-NH₁	NADH-N1N	3.3 ± 0.1	141.35 ± 13.16	31.20
	H ₂ O	NADH-O7N	2.8 ± 0.2	157.23 ± 13.05	100.0
	NADH-O3D	H ₂ O	3.0 ± 0.2	152.84 ± 11.65	83.05
	NADH-N7N	H ₂ O	3.2 ± 0.2	139.29 ± 13.35	66.00
	T479-Oγ1	NADH-O1A	2.6 ± 0.1	166.74 ± 07.32	99.98
	R905-NH ₁	NADH-O2N	2.8 ± 0.1	153.79 ± 11.58	98.60
NADH- <i>LmFR</i>	NADH-O2B	T669-O	2.9 ± 0.2	148.14 ± 15.12	54.30
	R742-NH₂	NADH-O2D	3.0 ± 0.2	149.15 ± 13.83	36.10
	R742-NH₁	NADH-O2D	3.1 ± 0.2	141.45 ± 10.71	18.30
	H ₂ O	NADH-O7N	2.8 ± 0.2	157.66 ± 12.89	100.0
	H ₂ O	NADH-O4D	3.0 ± 0.2	149.93 ± 15.02	81.14
	H ₂ O	NADH-O2N	2.8 ± 0.2	164.56 ± 08.76	67.64
	H ₂ O	NADH-N7A	2.9 ± 0.2	153.79 ± 14.34	65.86
	NADH-N7N	H ₂ O	3.2 ± 0.2	144.61 ± 15.01	63.56

^a Atom labeling according to Fig. 1A.^b Interactions evidenced in bold characters correspond to the putative catalytic residues (arginine R762 or R742, respectively, for *TcFR* and *LmFR*).

the nicotinamide moiety, onto the B-face of the ring (Fig. 6). This further supports the hypothesis that this residue could be assisting in the positioning of the substrate above the nicotinamide ring, being likely to serve as a proton donor toward fumarate, as it happens with residues R402(R401) in *Shewanella figidimarine* (*S. putrefaciens*). Thus, R762 could act in concert with hydride transfer from NADH to reduce the carbon–carbon double bond of the substrate, a possibility that is further discussed in the next section.

3.3. Substrate docking to NADH-enzyme models and refinement by MD simulations

In order to get a detailed scenario of the residues involved in the environment catalyzing fumarate reduction to succinate, the substrate was docked into the active site corresponding to each of the averaged structures obtained for both NADH-FRs. 1 ns MD simulations were run, reaching stabilization after 50 ps in both cases (see Fig. S4 in the Supplementary Material for the evolution of the total energy along the simulation). As illustrated in Fig. 7 and supported by the numerical information collected in Table 2, fumarate is maintained in the proposed binding site all along the simulation, with its two carboxylate groups stabilized by putative hydrogen bond interactions involving protein residues, the NADH cofactor, and some water molecules.

Whereas a pattern of high occupancy interactions between O₄ and the diol in the nicotinamide's ribosyl moiety is shared by both enzymes, some differences are noticed among them in terms of stabilizing interactions established by fumarate at the active site pocket. From one side, while all the four oxygen atoms in the dicarboxylate interact with water molecules present at the binding site of both enzymes, the O₄–water hydrogen bond in *LmFR* would be considerably more labile than the other carboxylate–water interactions. On the other side, a hydrogen bond is established in *TcFR* between O₁ and R762 through the NH₁ group, interaction that is absent in *LmFR*.

Along the simulation the substrate is positioned right above and near parallel to the cofactor's nicotinamide plane in both enzymes (a fact that might give support here to the idea of an orbital steering mechanism, like the one recently proposed for membrane-bound FAD-dependent FRs [25]) with mean distance values of 4.5 ± 0.2 Å (*TcFR*) and 3.6 ± 0.2 Å (*LmFR*) taken from C₂ in the C₂=C₃ double bond of fumarate and C₄ in the nicotinamide ring. The distance between NH₁ in the putative catalytic residue R762(R742) and C₃ in the substrate is 4.3 ± 0.3 Å in *TcFR* and 3.5 ± 0.4 Å in *LmFR*. The evolution of these parameters along the MD simulation is shown in Fig. 8.

These observations would be all compatible with a global picture of the mechanism involving the nicotinamide moiety of NADH

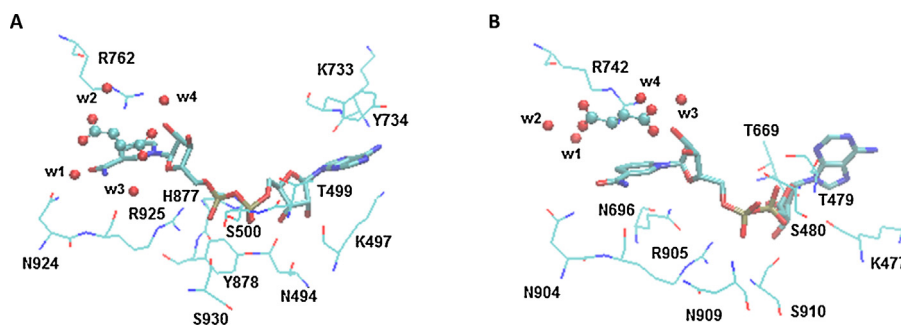


Fig. 7. Substrate positioning in the active site of *NADH-TcFR* (A) and *NADH-LmFR* (B). Averaged structures obtained with *ptraj* from the 150–1000 ps MD time frame. NADH is depicted as sticks, fumarate as ball & sticks, protein residues in contact with NADH are depicted as line representations, and water molecules (w1–w4) involved in persistent H-bonding are represented as red balls. (For interpretation of the references to color in this figure legend, the reader is referred to the web version of the article.)

Table 2
Hydrogen bond contacts established by fumarate along the MD simulation.

Ternary complex	H-donor ^a (residue-atom)	HB-acceptor ^a	Distance (Å)	Angle (°)	Occupancy (%)
<i>TcFR</i>	H ₂ O w1	O1	2.8 ± 0.3	155.74 ± 15.45	100.0
	H ₂ O w2	O2	2.8 ± 0.2	156.55 ± 14.94	100.0
	H ₂ O w3	O3	2.8 ± 0.2	159.85 ± 12.07	100.0
	H ₂ O w4	O4	2.9 ± 0.3	152.43 ± 16.62	100.0
	NADH-O3D	O4	2.7 ± 0.1	165.13 ± 08.40	98.58
	NADH-O2D	O4	2.8 ± 0.1	159.45 ± 11.47	97.60
	R762-NH1	O1	2.9 ± 0.2	167.33 ± 12.67	90.94
<i>LmFR</i>	H ₂ O w1	O1	2.8 ± 0.2	157.47 ± 14.68	100.0
	H ₂ O w2	O2	2.8 ± 0.2	157.49 ± 14.14	100.0
	H ₂ O w3	O3	2.5 ± 0.2	159.76 ± 12.64	100.0
	H ₂ O w4	O4	2.8 ± 0.3	151.05 ± 15.94	37.28
	NADH-O3D	O4	2.7 ± 0.1	162.81 ± 09.62	99.16
	NADH-O2D	O4	2.6 ± 0.1	158.77 ± 11.07	98.38

^a Atom labeling according to Fig. 1B.

placed at a distance and orientation adequate for a hydride transfer to fumarate C₂=C₃ while the R762(R742) side chain is also well oriented to act as a proton donor during the catalytic cycle. To be also taken into consideration here is that fumarate retains the planar conformation during the simulation (as expected by using a classical description of the system). Describing the eventual formation of a twisted intermediate – invoked in both membrane-bound and soluble FAD-dependent FRs as way of promoting hydride transfer from the cofactor [25,71] – would require the use of more sophisticated quantum models of the reactive system, capable of describing bond breaking/formation and electron displacements, a kind of study that goes further the scope of the present work.

3.4. Molecular docking of known and potential *TcFR* and *LmFR* inhibitors

The averaged structural models of the NADH cofactor-enzyme complexes obtained from the MD simulations with the features discussed in Section 3.2 were used here to explain/predict the inhibitory capacity and binding modes for a set of ligands that include both known inhibitors of *TcFR* or *LmFR* as well as species considered as potential inhibitors. [Pt(mpo)₂] and [Pd(mpo)₂] metal complexes are known inhibitors of *TcFR* [27] used to validate the model by molecular docking into the NADH-*TcFR* complex, study that is extended to [VO(mpo)₂] as a potential inhibitor [28]. Licochalcone A was in turn taken as the known inhibitor of the enzyme of *L. major* [23] used here to test the predictability of the NADH-*LmFR* model toward exploring the performance of the three metal-mpo complexes as *LmFR* inhibitors and to gain insight into the molecular mechanism explaining its known inhibitory power.

Table 3

Theoretical inhibition constants (*K_i*) and experimental IC₅₀ values obtained for *TcFR* and *LmFR* inhibition.

Ligand	<i>TcFR</i>		<i>LmFR</i>	
	<i>K_i</i> (μM)	IC ₅₀ (μM) ^{a,d}	<i>K_i</i> (μM)	IC ₅₀ (μM) ^b
[Pt(mpo) ₂]	101	>200	131	na ^c
[Pd(mpo) ₂]	79.3	200	122	na ^c
[VO(mpo) ₂]	109	na ^c	111	na ^c
Licochalcone A	–	–	13.2	14.0

^a From Ref. [27].

^b From Ref. [23].

^c Data not available.

^d Inhibition of *TcFR* by Na(mpo) was assessed under identical conditions than for mpo-chelates using a fixed dose of 225 μM for each species (as reported in ref. 27) showing that whereas all of them inhibited the enzyme [Pd(mpo)₂] was twice more potent respect to free mpo and [Pt(mpo)₂] (which displayed a similar degree of inhibitory activity as compared to the free ligand).

Such a knowledge will be useful in the rational design of new anti-trypanosomatid agents.

As displayed in Table 3, the theoretical inhibition constants (*K_i* values as calculated by Autodock 4.0 from the binding free energies) obtained correlate well with the available experimental data, showing that the structural models can be in fact used as scaffolds for virtual screening purposes. Considering the theoretical values, in principle no improvement in the inhibitory activity against *TcFR* is expected for [VO(mpo)₂], nor a better performance respect to licochalcone A is expectable for each of the three metal-mpo complexes acting as *LmFR* inhibitors, being the oxidovanadium species predicted as the most effective among them. According to the picture emerging from the molecular docking of these known

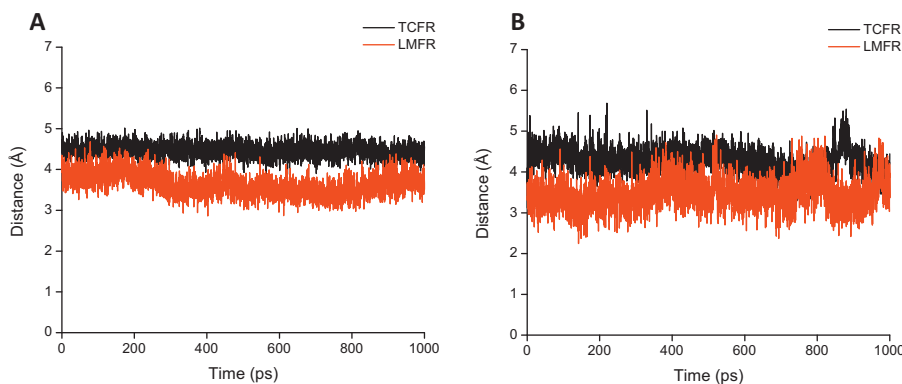


Fig. 8. Evolution of the distance among moieties presumed to be involved in the catalytic mechanism along the MD simulations run for the ternary complexes of *TcFR* (black profiles) and *LmFR* (red profiles). (A) Fumarate C₂=C₃...C4 NADH nicotinamide ring. (B) Fumarate C₂=C₃...NH1 at R762(R742). (For interpretation of the references to color in this figure legend, the reader is referred to the web version of the article.)

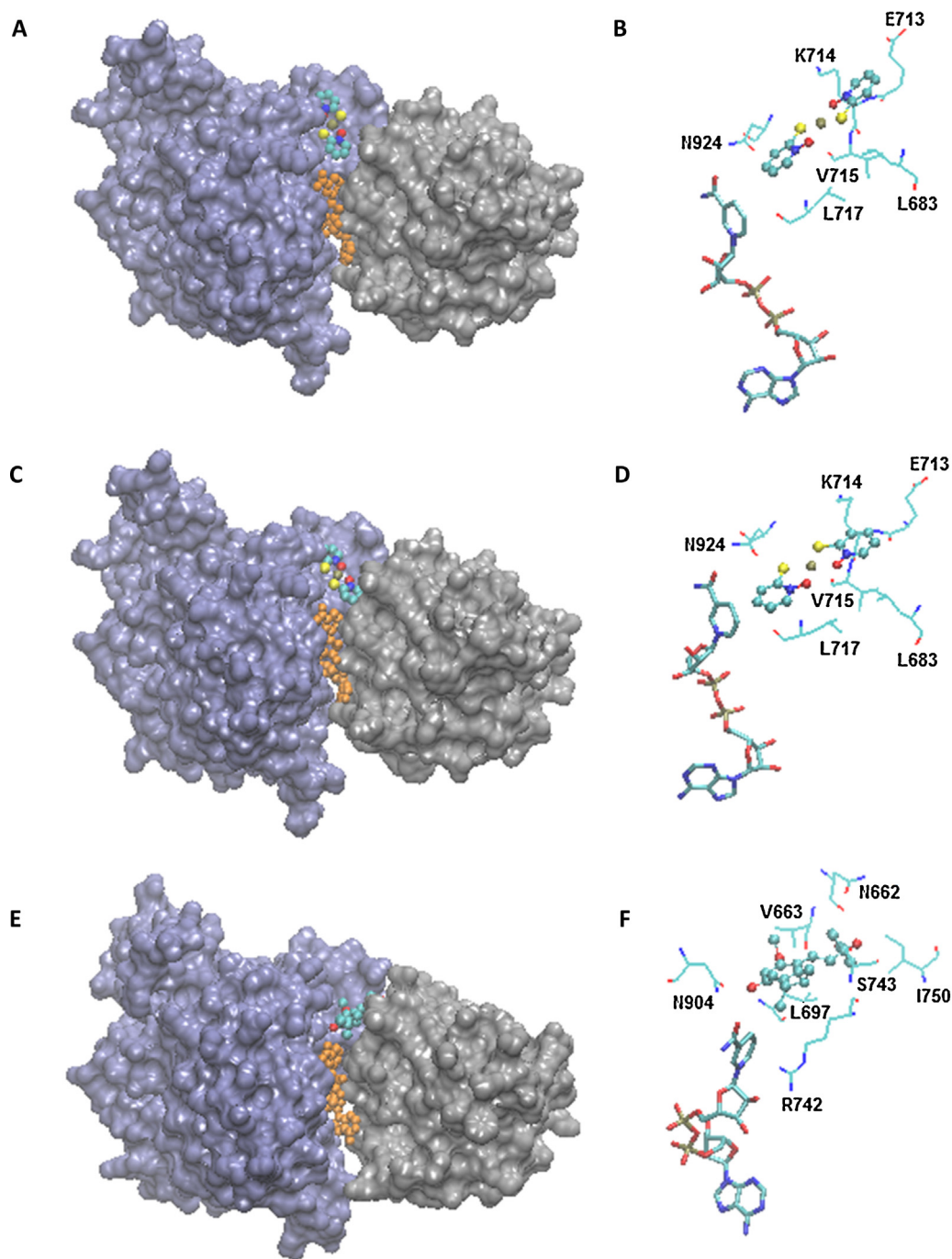


Fig. 9. Predicted binding mode (left) and close-up view of the contact residues within 3.5 Å of each species (right) around the binding site of known inhibitors of *TcFR* ([Pt(mpo)₂] (A and B) and [Pd(mpo)₂] (C and D)) and of *LmFR* (Licochalcone A (E and F)). Coloring scheme for the SASA representations in (A, C, E): domain 2 – iceblue; domain 3 – silver; NADH represented as vdW orange overlapped spheres. (For interpretation of the references to color in this figure legend, the reader is referred to the web version of the article.)

inhibitors to the NADH-FR complexes (see Fig. 9) all the species bind into the cleft between domains 2 and 3 in both enzymes, positioning close to the nicotinamide ring of the NADH cofactor.

As depicted in Fig. 9A/B, [Pt(mpo)₂] is stabilized in the binding site of *TcFR* by hydrophobic interactions with L683, V715, L717 and the aliphatic C in the side chain of K714. Located at a distance of 2.8 Å, the metallic center is suitably positioned to coordinate with the main chain oxygen atom of V715. Although this compound does not make direct contacts with residues involved in the NADH binding, the location at the interface between domains could be altering this region causing an improper binding of the cofactor.

The binding mode of [Pd(mpo)₂] to *TcFR* appears to be similar to that of the Pt analog (Fig. 9C/D). However, it stays closer to the cofactor, establishing a repulsive interaction between a sulfur atom from one mpo moiety and the main chain oxygen of N924. This interaction could be promoting a different orientation of residue N924 which, as mentioned in Section 3.2, plays a key role in orienting the nicotinamide ring in a proper position for catalysis. This fact could explain the better inhibitory capacity against *TcFR* displayed by [Pd(mpo)₂].

The nature of the interaction of Licochalcone A at the binding site of *LmFR* is shown in Fig. 9E/F. This potent inhibitor (see Table 3)

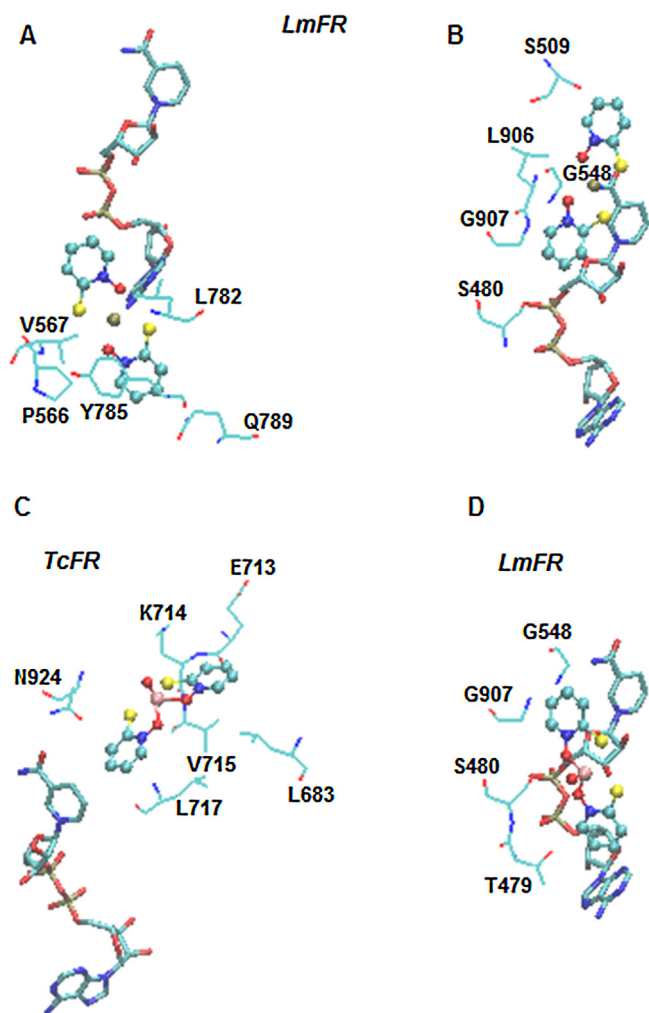


Fig. 10. Docking results for potential inhibitors of *TcFR* and *LmFR*. (A) and (B) represent the binding site of $[\text{Pt}(\text{mpo})_2]$ and $[\text{Pd}(\text{mpo})_2]$ in *LmFR*; (C) and (D) correspond to $[\text{VO}(\text{mpo})_2]$ bound into *TcFR* and *LmFR*, respectively.

establishes hydrophobic interactions with V663, L697, I750 and the aliphatic carbons in the side chain of R742. Additionally, whereas one of its phenol OHs establishes a hydrogen bond with atom O δ 1 from N904, its second OH interacts with the carbonyl oxygen at the backbone of N662 and the C=O group from the chalcone also interacts with atom O γ 1 from S743. In summary, Licochalcone A would interact with the side chains of residues found to be key for the FR activity, combining the ability of altering both the cofactor binding and positioning and interfering with fumarate positioning and reduction at the catalytic site. These two aspects could be in the center of an explanation of the potent inhibitory activity of the compound against *LmFR*.

As can be seen in Fig. 10A, the binding site for $[\text{Pt}(\text{mpo})_2]$ in *LmFR* is completely different from the one corresponding to *TcFR* (Fig. 9A). In *LmFR* this metal complex binds near the adenosine end of NADH through π – π stacking interactions with the phenolic side chain of Y785. O and S atoms from the same side of this trans Pt(II) species interact through HB with the N $_{6A}$ atom in the adenosine moiety. Hence, binding of $[\text{Pt}(\text{mpo})_2]$ at this location might alter the NADH–*LmFR* association, causing a lower inhibition in comparison to *TcFR* due to its location far away from the active site.

$[\text{Pd}(\text{mpo})_2]$ binds to *LmFR* close to the nicotinamide ring of the cofactor, but in a different site than the one observed in *TcFR* (Fig. 10B). The main interactions stabilizing the compound are hydrogen bonds established between the oxygen atoms of the mpo

coordinated ligands and N $_{7N}$ in the nicotinamide ring. Although $[\text{Pd}(\text{mpo})_2]$ binds closer to the catalytic pocket, the compound is placed quite distant from the catalytic face of the nicotinamide ring and hence it would be expected to be a worse inhibitor of this enzyme relative to *TcFR*, which is consistent with the theoretical K_i values.

Concerning the oxidovanadium derivative, the results collected in Table 3 present this compound as a mild inhibitor of both enzymes. Fig. 10C illustrates a binding mode for $[\text{VO}(\text{mpo})_2]$ in *TcFR* quite similar to that observed for the corresponding Pt analog in the same enzyme. Therefore both compounds could be acting through a similar mechanism, probably disrupting the interface between domains, affecting somehow the correct orientation of the cofactor as needed to properly take part in the catalytic cycle. On the other hand, $[\text{VO}(\text{mpo})_2]$ binds to *LmFR* in a different site but establishing hydrogen bond interactions between an oxygen atom of one mpo moiety and the S480 residue. At the same time the O $_{3D}$ atom in the nicotinamide ribose interacts through a hydrogen bond with a sulfur atom of mpo. Thus, $[\text{VO}(\text{mpo})_2]$ might disrupt the HB network that helps to maintain a proper positioning of the cofactor at its binding site.

4. Conclusions

This study constitutes the first attempt made to elucidate the structure of NADH-dependent fumarate reductases from *Trypanosoma cruzi* and *Leishmania major*. The high sequence similarity found between *TcFR* and *LmFR* and other soluble FRs and a sub-cellular localization analysis suggest that these parasitic enzymes are soluble and (at least in part) extra-mitochondrial as already described for *T. brucei* NADH-FR. 3D models of the apoenzymes were constructed by integrating homology modeling of the central domains containing the conserved residues in the putative active site, followed by enzyme-cofactor docking and refinement/validation with MD simulations. Insight is thus gained on the binding mode of NADH in each protein, as well as on the interactions the substrate (fumarate) establishes at the putative active site, characterized from 3D ternary complexes modeled by using a similar protocol. NADH-FR models were used here to analyze docking areas for metal-mpo complexes and Licochalcone A as known inhibitors of *TcFR* and *LmFR*. The results thus obtained are consistent with the data reported on the FR inhibitory activity of the species, showing the value of this information and models for future use in the structure-based design of new anti-trypanosomatids.

Acknowledgements

The authors are grateful to Prof. A. Divsalar (Institute of Biochemistry and Biophysics, University of Tehran, Tehran, Iran) and Dr. R.H. Sarma (Department of Chemistry and Biological Sciences, State University of New York, Albany, USA) for providing the set of AutoDock force field parameters for Pd(II). The Program of Development of the Basic Sciences (PEDECIBA–Química, UDELAR–UNDP – Uruguayan government) is also gratefully acknowledged for financial support.

All the authors are members of the National System of Researchers (SNI–ANII, Uruguay) whose support is also gratefully acknowledged.

Appendix A. Supplementary data

Supplementary data associated with this article can be found, in the online version, at <http://dx.doi.org/10.1016/j.jmgm.2013.12.001>.

References

- [1] M.P. Barret, R.J.S. Burchmore, A. Stich, J.O. Lazzari, A.C. Frasch, J.J. Cazzulo, S. Krishna, The trypanosomiasis, *Lancet* 362 (2003) 1469–1480.
- [2] World Health Organization, Chagas disease (American Trypanosomiasis) fact sheet N°340, August 2012 (accessed 18.12.2012) <http://www.who.int/mediacentre/factsheets/fs340/en/index.html>
- [3] J.R. Coura, S.L. de Castro, A critical review on Chagas disease chemotherapy, *Mem. Inst. Oswaldo Cruz* 97 (2002) 3–24.
- [4] L.V. Kirchhoff, R.D. Pearson, The emergence of Chagas disease in the United States and Canada, *Curr. Infect. Dis. Rep.* 9 (2007) 347–350.
- [5] D. Dobarro, C. Gomez-Rubin, A. Sanchez-Recalde, F. Olias, M. Bret-Zurita, E. Cuesta-Lopez, A. Robles-Marhuenda, J.M. Fraile-Vicente, J.R. Pano-Pardo, J. Lopez-Sendon, Chagas' heart disease in Europe: an emergent disease? *J. Cardiovasc. Med.* 9 (2008) 1263–1267.
- [6] World Health Organization, Leishmaniasis: epidemiology and access to medicines – an update based on the outcomes of WHO regional meetings, literature review and experts' opinion, May 2012 (accessed 18.12.2012) http://www.who.int/leishmaniasis/resources/Leishmaniasis.worldwide_epidemiological_and_drug_access_update.pdf
- [7] J.A. Urbina, New insights in Chagas' disease treatment, *Drugs Future* 35 (2010) 409–419.
- [8] H. Cerecetto, M. González, Chemotherapy of Chagas' disease: status and new developments, *Curr. Top. Med. Chem.* 2 (2002) 1185–1211.
- [9] J.A. Marin-Neto, A. Rassi Jr., A. Avezum Jr., A.C. Mattos, A. Rassi, The benefit trial: testing the hypothesis that trypanocidal therapy is beneficial for patients with chronic Chagas heart disease, *Mem. Inst. Oswaldo Cruz* 104 (2009) 319–324.
- [10] I. Ribeiro, A.M. Sevcik, F. Alves, G. Diap, R. Don, M.O. Harhay, S. Chang, B. Pecoul, New, improved treatments for Chagas disease: from the R&D Pipeline to the patients, *PLoS Negl. Trop. Dis.* 3 (2009) e484.
- [11] R.A. Sánchez-Delgado, A. Anzellotti, Metal complexes as chemotherapeutic agents against tropical diseases: trypanosomiasis, malaria, and leishmaniasis, *Mini-Rev. Med. Chem.* 1 (2004) 23–30.
- [12] L. Monzote, Current treatment of leishmaniasis: a review, *Open Antimicrob. Agents J.* 1 (2009) 9–19.
- [13] S.L. Croft, G.H. Coombs, Leishmaniasis – current chemotherapy and recent advances in the search for novel drugs, *Trends Parasitol.* 19 (2003) 502–508.
- [14] A. Merlino, M. González, H. Cerecetto, Targets for anti-*T. cruzi* drugs in the post genomic era, *Curr. Enzyme Inhib.* 6 (2010) 195–210.
- [15] S. Malik, S. Kumar, A. Choudhary, A. Kumar, A. Singh, G. Avasthi, Leishmaniasis: current treatment strategies and future opportunities, *J. Chem. Pharm. Res.* 2 (2010) 70–91.
- [16] G.J. Crowther, D. Shanmugam, S.J. Carmona, M.A. Doyle, C. Hertz-Fowler, M. Berriman, S. Nwaka, S.A. Ralph, D.S. Roos, W.C. Van Voorhis, F. Agüero, Identification of attractive drugs targets in neglected-disease pathogens using an *in silico* approach, *PLoS Negl. Trop. Dis.* 4 (2010) e804.
- [17] A. Denicola-Seoane, H. Rubbo, E. Prodanov, J.F. Turrens, Succinate-dependent metabolism in *Trypanosoma cruzi* epimastigotes, *Mol. Biochem. Parasitol.* 54 (1992) 43–50.
- [18] M. Chen, M. Bennedsen, L. Zhai, A. Kharazmi, Purification and enzymatic activity of an NADH-fumarate reductase and other mitochondrial activities of *Leishmania* parasites, *APMIS* 109 (2001) 801–808.
- [19] S. Besteiro, M. Biran, N. Bateau, V. Coustou, T. Baltz, P. Canioni, F. Bringaude, Succinate secreted by *Trypanosoma brucei* is produced by a novel and unique glycosomal enzyme NADH-dependent fumarate reductase, *J. Biol. Chem.* 277 (2002) 38001–38012.
- [20] V. Coustou, S. Besteiro, L. Rivière, M. Biran, N. Bateau, J.M. Franconi, M. Boshart, T. Baltz, F. Bringaude, A mitochondrial NADH-dependent fumarate reductase involved in the production of succinate excreted by procyclic *Trypanosoma brucei*, *J. Biol. Chem.* 280 (2005) 16559–16570.
- [21] J.F. Turrens, B.P. Watts Jr., L. Zhong, R. Docampo, Inhibition of *Trypanosoma cruzi* and *T. brucei* NADH fumarate reductase by benzimidazole and anthelmintic imidazole derivatives, *Mol. Biochem. Parasitol.* 82 (1996) 125–129.
- [22] J.F. Turrens, C.L. Newton, L. Zhong, F.R. Hernández, J. Whitfield, R. Docampo, Mercaptopuridine-*N*-oxide an NADH-fumarate reductase inhibitor blocks *Trypanosoma cruzi* growth in culture and in infected myoblasts, *FEMS Microbiol. Lett.* 175 (1999) 217–221.
- [23] M. Chen, L. Zhai, S.B. Christensen, T.G. Theander, A. Kharazmi, Inhibition of fumarate reductase in *Leishmania major* and *L. donovani* by chalcones, *Antimicrob. Agents Chemother.* 45 (2001) 2023–2029.
- [24] O. Kayser, M. Chen, A. Kharazmi, A.F. Kiderlen, Aurones interfere with leishmania major mitochondrial fumarate reductase, *Z. Naturforsch. C: J. Biosci.* 57 (2002) 717–720.
- [25] T.M. Iverson, Catalytic mechanisms of complex II enzymes: a structural perspective, *Biochim. Biophys. Acta* (2012), <http://dx.doi.org/10.1016/j.bbabi.2012.09.008> (in press).
- [26] C. Sakai, E. Tomitsuka, H. Esumi, S. Harada, K. Kita, Mitochondrial fumarate reductase as a target of chemotherapy: from parasites to cancer cells, *Biochim. Biophys. Acta* 1820 (2012) 643–651.
- [27] M. Vieites, P. Smircich, B. Parajón-Costa, J. Rodríguez, V. Galaz, C. Olea-Azar, L. Otero, G. Aguirre, H. Cerecetto, M. González, A. Gómez-Barrio, B. Garat, D. Gambino, Potent *in vitro* anti-*Trypanosoma cruzi* activity of pyridine-2-thiol *N*-oxide metal complexes having an inhibitory effect on parasite-specific fumarate reductase, *J. Biol. Inorg. Chem.* 13 (2008) 723–735.
- [28] D. Gambino, Potentiality of vanadium compounds as anti-parasitic agents, *Coord. Chem. Rev.* 255 (2011) 2193–2203.
- [29] E. Boutet, D. Lieberherr, M. Tognolli, M. Schneider, A. Bairoch, UniProtK.B/Swiss-Prot: the manually annotated section of the UniProt Knowledge Base, *Methods Mol. Biol.* 406 (2007) 89–112.
- [30] S.F. Altschul, J.C. Wootton, E.M. Gertz, R. Agarwala, A. Morgulis, A.A. Schäffer, Y.K. Yu, Protein database searches using compositionally adjusted substitution matrices, *FEBS J.* 272 (2005) 5101–5109.
- [31] J.D. Thompson, D.G. Higgins, T.J. Gibson, CLUSTAL W: improving the sensitivity of progressive multiple sequence alignment through sequence weighting, position-specific gap penalties and weight matrix choice, *Nucleic Acids Res.* 22 (1994) 4673–4680.
- [32] T. Schwede, J. Kopp, N. Guex, M.C. Peitsch, SWISS-MODEL: an automated protein homology-modeling server, *Nucleic Acids Res.* 31 (2003) 3381–3385.
- [33] R. Maiti, G.H. Van Domselaar, H. Zhang, D.S. Wishart, SuperPose: a simple server for sophisticated structural superposition, *Nucleic Acids Res.* 32 (2004) W590–W594.
- [34] (a) R.A. Laskowski, M.W. MacArthur, D.S. Moss, J.M. Thornton, PROCHECK: a program to check the stereochemical quality of protein structures, *J. Appl. Cryst.* 26 (1993) 283–291;
(b) V.B. Chen, W.B. Arendall III, J.J. Headd, D.A. Keedy, R.M. Immormino, G.J. Kapral, L.W. Murray, J.S. Richardson, D.C. Richardson, MolProbity: all-atom structure validation for macromolecular crystallography, *Acta Crystallogr. D* 66 (2010) 12–21.
- [35] R. Luthy, J.U. Bowie, D. Eisenberg, Assessment of protein models with 3-dimensional profiles, *Nature* 356 (1992) 83–85.
- [36] Y. Duan, C. Wu, S. Chowdhury, M.C. Lee, G. Xiong, W. Zhang, R. Yang, P. Cieplak, R. Luo, T. Lee, J. Caldwell, J. Wang, P. Kollman, A point-charge force field for molecular mechanics simulations of proteins based on condensed-phase quantum mechanical calculations, *J. Comput. Chem.* 24 (2003) 1999–2012.
- [37] D.A. Case, T.A. Darden, T.E. Cheatham III, C.L. Simmerling, J. Wang, R.E. Duke, R. Luo, R.C. Walker, W. Zhang, K.M. Merz, B. Roberts, S. Hayik, A. Roitberg, G. Seabra, J. Swails, A.W. Goetz, I. Kolossvai, K.F. Wong, F. Paesani, J. Vanicek, R.M. Wolf, J. Liu, X. Wu, S.R. Brozell, T. Steinbrecher, H. Gohlke, Q. Cai, X. Ye, J. Wang, M.-J. Hsieh, G. Cui, D.R. Roe, D.H. Mathews, M.G. Seetin, R. Salomon-Ferrer, C. Sagui, V. Babin, T. Luchko, S. Gusarov, A. Kovalenko, P.A. Kollman, AMBER 12, University of California, San Francisco, 2012.
- [38] A. Onufriev, D. Bashford, D.A. Case, Exploring protein native states and large-scale conformational changes with a modified generalized Born model, *Proteins* 55 (2004) 383–394.
- [39] A.D. Becke, Density-functional exchange-energy approximation with correct asymptotic behavior, *Phys. Rev. A* 38 (1988) 3098–3100.
- [40] J.P. Perdew, Density-functional approximation for the correlation energy of the inhomogeneous electron gas, *Phys. Rev. B* 33 (1986) 8822–8824.
- [41] T. Clark, J. Chandrasekhar, P.V.R. Schleyer, Efficient diffuse function-augmented basis sets for anion calculations. III. The 3-21+G basis set for first-row elements Li–F, *J. Comput. Chem.* 4 (1983) 294–301.
- [42] R. Krishnam, J.S. Binkley, R. Seeger, J.A. Pople, Self-consistent molecular orbital methods. XX. A basis set for correlated wave functions, *J. Chem. Phys.* 72 (1980) 650–654.
- [43] P.J. Hay, W.R. Wadt, Ab initio effective core potentials for molecular calculations. Potentials for the transition metal atoms Sc to Hg, *J. Chem. Phys.* 82 (1985) 270–283.
- [44] P.J. Hay, W.R. Wadt, Ab initio effective core potentials for molecular calculations. Potentials for K to Au including the outermost core orbitals, *J. Chem. Phys.* 82 (1985) 299–310.
- [45] M.J. Frisch, G.W. Trucks, H.B. Schlegel, G.E. Scuseria, M.A. Robb, J.R. Cheeseman, G. Scalmani, V. Barone, B. Mennucci, G.A. Petersson, H. Nakatsuji, M. Caricato, X. Li, H.P. Hratchian, A.F. Izmaylov, J. Bloino, G. Zheng, J.L. Sonnenberg, M. Hada, M. Ehara, K. Toyota, R. Fukuda, J. Hasegawa, M. Ishida, T. Nakajima, Y. Honda, O. Kitao, H. Nakai, T. Vreven, J.A. Montgomery Jr., J.E. Peralta, F. Ogliaro, M. Bearpark, J.J. Heyd, E. Brothers, K.N. Kudin, V.N. Staroverov, R. Kobayashi, J. Normand, K. Raghavachari, A. Rendell, J.C. Burant, S.S. Iyengar, J. Tomasi, M. Cossi, N. Rega, J.M. Millam, M. Klene, J.E. Knox, J.B. Cross, V. Bakken, C. Adamo, J. Jaramillo, R. Gomperts, R.E. Stratmann, O. Yazyev, A.J. Austin, R. Cammi, C. Pomelli, J.W. Ochterski, R.L. Martin, K. Morokuma, V.G. Zakrzewski, G.A. Voth, P. Salvador, J.J. Dannenberg, S. Dapprich, A.D. Daniels, Ö. Farkas, J.B. Foresman, J.V. Ortiz, J. Cioslowski, D.J. Fox, Gaussian 09, Revision A.02, Gaussian Inc, Wallingford, CT, 2009.
- [46] G.M. Morris, R. Huey, W. Lindstrom, M.F. Sanner, R.K. Belew, D.S. Goodsell, A.J. Olson, AutoDock4 and AutoDockTools4: automated docking with selective receptor flexibility, *J. Comput. Chem.* 30 (2009) 2785–2791.
- [47] Autodock Forum, ADL, Parameters for docking with metal ions in receptor, 2012 (accessed August 2012). <http://autodock.1369657.n2.nabble.com/ADL-Parameters-for-docking-with-metal-ions-in-receptor-t2505649.html>
- [48] A. Divsalar, A.A. Saboury, L. Ahadi, E. Zemanatizadeh, H. Mansouri-Torshizi, D. Ajloo, R.H. Sarma, Biological evaluation and interaction of a newly designed anti-cancer Pd(II) complex and human serum albumin, *J. Biomol. Struct. Dyn.* 29 (2011) 283–296.
- [49] J. Wang, R.M. Wolf, J.W. Caldwell, P.A. Kollman, D.A. Case, Development and testing of a general AMBER force field, *J. Comput. Chem.* 25 (2004) 1157–1174.
- [50] Amber Parameter Database, Prof. Richard Bryce, University of Manchester. <http://www.pharmacy.manchester.ac.uk/bryce/amber/> (accessed May 2012).
- [51] C.M. Breneman, K.B. Wiberg, Determining atom-centered monopoles from molecular electrostatic potentials—the need for high sampling density in formamide conformational-analysis, *J. Comput. Chem.* 11 (1990) 361–373.

- [52] W.L. Jorgensen, J. Chandrasekhar, J.D. Madura, R.W. Impey, M.L. Klein, Comparison of simple potential functions for simulating liquid water, *J. Chem. Phys.* 79 (1983) 926–935.
- [53] U. Essmann, L. Perera, M.L. Berkowitz, T. Darden, H. Lee, L.G. Pedersen, A smooth particle mesh Ewald method, *J. Chem. Phys.* 103 (1995) 8577–8593.
- [54] P.H. Hünenberger, Thermostat algorithms for molecular dynamics simulations, *Adv. Polym. Sci.* 173 (2005) 105–149.
- [55] J.P. Ryckaert, G. Ciccotti, H.J.C. Berendsen, Numerical-integration of Cartesian equations of motion of a system with constraints – molecular-dynamics of *n*-alkanes, *J. Comput. Phys.* 23 (1977) 327–341.
- [56] T.N. Petersen, S. Brunak, G. von Heijne, H. Nielsen, SignalP 4.0: discriminating signal peptides from transmembrane regions, *Nat. Methods* 8 (2011) 785–786.
- [57] K. Laurila, M. Vihinen, PROlocalizer: integrated web service for protein subcellular localization prediction, *Amino Acids* 40 (2011) 975–980.
- [58] B. Cao, A. Porollo, R. Adamczak, M. Jarrell, J. Meller, Enhanced recognition of protein transmembrane domains with prediction-based structural profiles, *Bioinformatics* 22 (2006) 303–309.
- [59] M.G. Claros, P. Vincens, Computational method to predict mitochondrially imported proteins and their targeting sequences, *Eur. J. Biochem.* 241 (1996) 779–786.
- [60] S. Maurer-Stroh, B. Eisenhaber, F. Eisenhaber, N-terminal *N*-myristoylation of proteins: prediction of substrate proteins from amino acid sequence, *J. Mol. Biol.* 317 (2002) 541–557.
- [61] D.T. Jones, Protein secondary structure prediction based on position-specific scoring matrices, *J. Mol. Biol.* 292 (1999) 195–202.
- [62] D.T. Jones, J.J. Ward, Prediction of disordered regions in proteins from position specific score matrices, *Proteins* 53 (2003) 573–578.
- [63] L.A. Kelley, M.J.E. Sternberg, Protein structure prediction on the web: a case study using the Phyre server, *Nat. Protoc.* 4 (2009) 363–371.
- [64] P. Taylor, S.L. Pealing, G.A. Reid, S.K. Chapman, M.D. Walkinshaw, Structural and mechanistic mapping of a unique fumarate reductase, *Nat. Struct. Biol.* 6 (1999) 1108–1112.
- [65] T.M. Iverson, C. Luna-Chavez, G. Cecchini, D.C. Rees, Structure of the *Escherichia coli* fumarate reductase respiratory complex, *Science* 284 (1999) 1961–1966.
- [66] C.R. Lancaster, A. Kröger, M. Auer, H. Michel, Structure of fumarate reductase from *Wolinella succinogenes* at 2.2 Å resolution, *Nature* 402 (1999) 377–385.
- [67] D. Leys, A.S. Tsapin, K.H. Nealon, T.E. Meyer, M.A. Cusanovich, J.J. Van Beeumen, Structure and mechanism of the flavocytochrome *c* fumarate reductase of *Shewanella putrefaciens* MR-1, *Nat. Struct. Biol.* 6 (1999) 1113–1117.
- [68] K.L. Pankhurst, C.G. Mowat, E.L. Rothery, J.M. Hudson, A.K. Jones, C.S. Miles, M.D. Walkinshaw, F.A. Armstrong, G.A. Reid, S.K. Chapman, A proton delivery pathway in the soluble fumarate reductase from *Shewanella frigidimarina*, *J. Biol. Chem.* 281 (2006) 20589–20597.
- [69] V. Leskovic, S. Trivić, D. Perićin, M. Popović, J. Kandrač, Binding of coenzymes to yeast alcohol dehydrogenase, *J. Serb. Chem. Soc.* 75 (2010) 185–194.
- [70] R.E. Johnson, J.A. Rupley, Binding of reduced and oxidized nicotinamide adenine dinucleotide to pig heart supernatant malate dehydrogenase, *Biochemistry* 18 (1979) 3611–3616.
- [71] M.F. Lucas, M.J. Ramos, Mechanism of a soluble fumarate reductase from *Shewanella frigidimarina*: a theoretical study, *J. Phys. Chem. B* 110 (2006) 10550–10556.